Article

Heat Source Modeling in Selective Laser Melting

Elham Mirkoohi [1],*, Daniel E. Seivers [2], Hamid Garmestani [3] and Steven Y. Liang [1]

[1] Woodruff School of Mechanical Engineering, Georgia Institute of Technology, Atlanta, GA 30332, USA; Elham.mirkoohi@gatech.edu

[2] Boeing Research and Technology, Ceramics, Extreme Environments & Metals, Huntsville, Al, 35824, USA; Daniel.E.Seivers@Boeing.com

[3] School of Materials Science and Engineering, Georgia Institute of Technology, Atlanta, GA 30332, USA; hamid.garmestani@mse.gatech.edu

* Correspondence: Elham.mirkoohi@gatech.edu

Abstract: Selective laser melting is an emerging Additive Manufacturing (AM) technology for metals. Intricate three-dimensional parts can be generated from the powder bed by selectively melting the desired location of the powders. The process is repeated for each layer until the part is built.   The necessary heat is provided by a laser. Temperature magnitude and history during SLM directly determine the molten pool dimensions, thermal stress, residual stress, balling effect, and dimensional accuracy. Laser-matter interaction is a crucial physical phenomenon in the SLM process. In this paper, five different heat source models are introduced to predict the three-dimensional temperature field analytically. These models are known as steady state moving point heat source, transient moving point heat source, semi-elliptical moving heat source, double elliptical moving heat source, and uniform moving heat source. The analytical temperature model for all of the heat source models are solved using three-dimensional differential equation of heat conduction with different approaches. The Steady state and transient moving heat source are solved using separation of variables approach. However, the rest of models are solved by employing the Green's functions. Due to the high magnitude of the temperature in the presence of the laser, the temperature gradient is usually high which has a substantial impact on thermal material properties. Consequently, the temperature field is predicted by considering the temperature sensitivity thermal material properties. Moreover, due to the repeated heating and cooling, the part usually undergoes several melting and solidification cycles, this physical phenomenon is considered by modifying the heat capacity using latent heat of melting. Furthermore, the multi-layer aspect of metal AM process is considered by incorporating the temperature history from the previous layer since the interaction of the layers have an impact on heat transfer mechanisms. The proposed temperature field models based on different heat source approaches are validated using experimental measurement of melt pool geometry from independent experimentations. The detailed explanation of the comparison of models is also provided. Moreover, the effect of process parameters on the balling effect is also discussed.

Keywords: temperature field; additive manufacturing; selective laser melting; heat source modeling

1. Introduction

Metal additive manufacturing (AM) processes are rapidly growing technologies that are utilized to build up 3D complex parts through a repetitive process of deposition of metallic powders and laser melting under the guidance of digital models [1, 2]. Compare to traditional manufacturing such as machining, rolling, casting and etc., these rapid prototyping techniques offers single step, net shape processing of complex parts, reduction of production time due to the elimination of multi-step manufacturing and reduction in cost due to the reduction in material scrap rate [3, 4].

Selective laser melting (SLM) process is the most common AM method for producing 3D complex, metallic structures [5]. The metallic micro-scale powders are liquified with a laser, forming a melt pool that penetrates through the previously deposited build layers, joining the layers upon cooling [6]. SLM is growing in many fields such as medical industries to manufacture bones,

49   implants, etc. [7]. Moreover, it is used in producing automobile and aerospace components to reduce
50   the final part density and weight, in order to reduce energy usage [8, 9].
51   Use of SLM parts in the industries, however, requires time-consuming flaw detection including
52   high residual stress induced crack initiation and growth [10, 11], undesired microstructures induced
53   undesired material properties [12], and high thermal stress induced delamination of the layers [13].
54   The main source of all abovementioned flaws in the SLM parts is a high temperature gradient
55   induced by laser. Therefore, accuracy in the modeling of the temperature field is of great importance.
56   To improve part quality, a thorough understanding of the real-time thermal characteristics is needed.
57   The complex multi-physics of the SLM process occurs at micro time and length scales. As a result
58   of complex phenomena involved in this process, relying on experimentation to understand the
59   underlying physical aspects of the SLM process alone would be too time consuming, costly, and
60   complex [14-16]. Numerical models such as finite element models and finite volume models are used
61   by many researchers, however, the simulation of the entire process could not be achieved in a
62   traceable amount of time. Consequently, many simplifications in modeling should be done [17-20].
63   In contrast, analytical models, validated by physical experiments provide a means of both effectively
64   understanding and optimizing the process by allowing for in-situ analysis as well as efficient
65   optimization of process parameters [15, 21, 22].
66   Several efforts have been made to model the temperature field in SLM process. These efforts can
67   be classified into three main categories known as experimentation, numerical modeling, and
68   analytical modeling.
69   Experimental work has been done to measure the in-situ temperature using different setups.
70   Thermocouples can be sited inside the substrate to measure the temperature [23, 24]. Due to the
71   existence of high temperature in metal AM, the thermocouple type K is recommended. It should be
72   noted that the thermocouples can only measure the temperature inside the substrate rather than the
73   build part. The thermal imager, Infrared (IR) camera, and pyrometer are the other available
74   technologies that can be used in measuring the in-situ temperature during AM process [25, 26]. More
75   information about different experimental setups can be found in different surveys [17, 27].
76   Numerical models such as finite element model (FEM) and finite volume model (FVM) are used
77   to simulate the AM process. Andreotta et al. employed a FEM to simulate the fluid flow and thermal
78   transport in metal AM using mass and momentum balance equations [28]. Roberts et al. developed a
79   3D FEM to predict the temperature field considering the multilayer aspect of metal AM. They
80   employed the element birth and death method to capture the addition of layers [29]. Antony et al.
81   developed a FEM to predict the temperature distribution in AISI 316L. They have studied the effect
82   of scan speed, laser power and beam size on temperature distribution [30]. Zohdi et al. developed a
83   discrete element model to simulate the deposition and heat transfer involved in the process of SLM
84   [31].
85   Mirkoohi et al. proposed a 2D physics-based analytical model to predict the temperature field
86   in the metal AM process. In the modeling of the temperature field, the effects of melting-solidification
87   phase change, layer addition, and temperature sensitive material properties are considered. The finite
88   element model (FEM) and also experimental work are used to validate the proposed analytical model
89   [32]. Pinkerton et al. proposed an analytical model to model the geometry of the melt pool. The model
90   considers the pool boundaries orthogonal to the direction of motion as arcs of a circle to account for
91   maximum surface tension and elongation of the melt pool at high speeds [33]. Peyer et al. employed
92   both analytical and numerical approaches to predict the shapes of manufacture structure and thermal
93   loadings in the direct metal deposition process. In their modeling, the powder temperature is
94   predicted using an analytical model, and analytical-numerical model is used to predict the geometry
95   [34]. Yang et al. proposed a semi-analytical model to predict the temperature during SLM process.
96   A point heat source model is discretized to laser scanning vectors and the evolution of the
97   temperature is predicted using superposition of the temperature field due to the discretized scanning
98   vectors [3]. Carslaw and Jaeger employed separation of variables approach to predict the temperature
99   field for the moving point heat source in a semi-infinite body [35].

100   The complex three-dimensional parts can be manufactured using SLM process by locally
101 melting the desired portion of the powders, layer by layer [36].The necessary heat for melting the
102 powders is provided by a laser. The laser-matter interaction is a crucial part in the modeling of the
103 SLM process. Various heat source modeling approaches exist in the literature to simulate the
104 temperature field during SLM process. Each of models has its own limitations, such as ignoring the
105 temperature sensitivity thermal material properties, ignoring the multi-layer aspect of metal AM,
106 ignoring the solid-state phase change. In this paper, five different analytical heat source modeling
107 approaches are introduced. The laser power and the scan speed are divided into three regions of high,
108 medium and low to investigate the ability of each of models in prediction of temperature field. The
109 predicted temperature fields are validated by experimental measurement of melt pool geometry [37-
110 39].
111   Moreover, the effect of process parameters on balling effect is also discussed. In this paper, the
112 single-track temperature field is predicted by considering the laser power absorptivity since it has a
113 direct influence on predicted melt pool temperature and geometry. Moreover, in the presence of the
114 laser, the temperature of the build part goes up to thousands of degrees and also the material
115 undergoes repeated heating and cooling, so, the material properties could change drastically.
116 Consequently, it is important to consider the temperature dependent thermal material properties.
117 Furthermore, the multi-layer aspect of metal AM could change the heat transfer mechanisms. As a
118 result, it has a substantial influence on predicted temperature field. Accordingly, the effect of the
119 addition of layers is also considered in the modeling as explained in previous work [32]. Due to the
120 repeated heating and cooling, the material undergoes a cyclic melting and solidification. This
121 repeated phase change has an impact on predicted temperature. Thus, to predict the temperature
122 field more accurately, the melting- solidification phase change is considered by modifying the heat
123 capacity using the latent heat of melting. This should be noted that the proposed models can be used
124 to predict the temperature in laser-based metal additive manufacturing configurations of either direct
125 metal deposition or selective laser melting.

126 **2. Methodology**

127   In this section, five different heat source modeling approaches are introduced to predict the
128 temperature field in laser-based metal AM process of SLM. The temperature field is predicted using
129 both steady-state moving heat source and transient moving heat source in a semi-infinite body. As
130 shown in Figure 1, the laser moves along the scan direction (x-axis) and deposited its energy to melt
131 the metallic powders. The heat loss due to convection and radiation is not considered in this
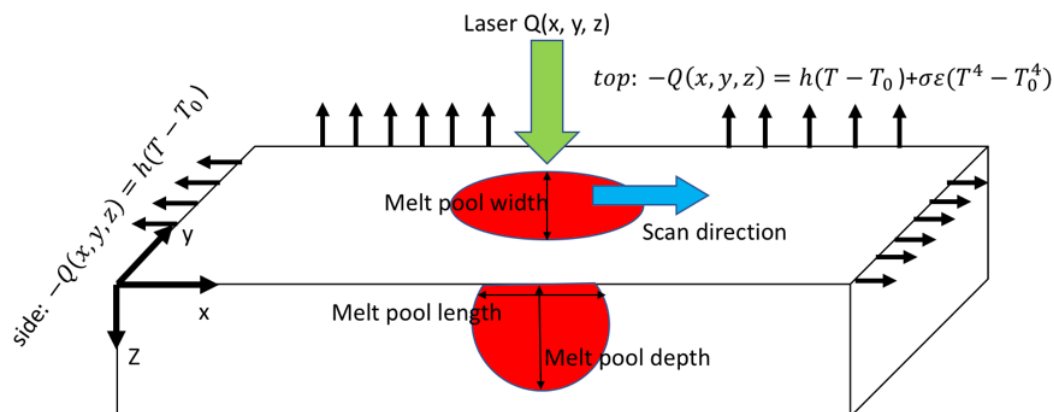132 modeling.

Figure 1. Illustration of the heat transfer model in laser bed metal additive manufacturing process.

135   Heat conduction in a homogeneous solid is governed by the linear partial differential equation

$$\frac{\partial u\rho}{\partial t} + \frac{\partial \rho hV}{\partial x} = \nabla.(k\nabla T) + \dot{q} \tag{1}$$

136 where u represents the internal energy, h is the enthalpy, ρ is the density, k is the
137 conductivity, $\dot{q}$ is a volumetric heat source, T is the temperature and V is the speed of either the heat
138 source or the medium.
139 The x direction corresponds to the constant speed of a moving heat source. Also, y is directed
140 inside the processed material, and z, the direction perpendicular to x in the plane of the processed
141 material surface. The first term in Eq. (1) on the left-hand side represents the change of internal energy
142 and the second is a convective term. On the right-hand side, there is the conductive term and a heat
143 source or sink. For $V = 0$, this equation becomes the heat conduction equation, given that du = C
144 dT, with C being the heat capacity

$$C\frac{\partial\rho T}{\partial t} + \frac{\partial\rho hV}{\partial x} = \nabla.(k\nabla T) + \dot{q} \tag{2}$$

145 The steady state equation with constant velocity V, can be simplified using the continuity
146 equation

$$C\frac{\partial\rho}{\partial t} + \frac{\partial\rho V}{\partial x} = 0 \tag{3}$$

147
148 Resulting in

$$\rho C(T)V\frac{\partial T}{\partial x} + \frac{\partial\rho hV}{\partial x} = \nabla.(k(T)\nabla T) + \dot{q} \tag{4}$$

149 given that du = dh = CdT.
150
151 The convection-diffusion equation becomes the differential equation of heat conduction which
152 can be expressed as
153

$$\frac{\partial^2 T}{\partial x^2} + \frac{\partial^2 T}{\partial y^2} + \frac{\partial^2 T}{\partial z^2} + \frac{1}{k}Q(x,y,z,t) = \frac{1}{D}\frac{\partial T}{\partial t} \tag{5}$$

154
155 where $T \equiv T(x,y,z,t)$. k is thermal conductivity, and D is the thermal diffusivity. The heat
156 source Q is related to the equivalent volumetric source $Q(x,y,z,t)$ (W/m³) by the delta function
157 notation as

$$Q(x,y,z,t) = Q\,\delta(x - Vt)\delta(y - y_0)\delta(z - z_0) \tag{6}$$

158 where δ denotes the Dirac delta function.
159 In order to consider the moving heat source, it is assumed that the coordinate system transfers
160 from the x,y,z fixed coordinate system to ζ,y,z coordinate moving by using the transformation
161

$$\zeta = x - Vt \tag{7}$$

162 Using the abovementioned transformation, the heat conduction equation for the moving
163 coordinate system can be written as

$$\frac{\partial^2 T}{\partial\zeta^2} + \frac{\partial^2 T}{\partial y^2} + \frac{\partial^2 T}{\partial z^2} + \frac{1}{k}Q\delta(\zeta)\delta(y)\delta(z) = \frac{1}{D}\left(\frac{\partial T}{\partial t} - V\frac{\partial T}{\partial\zeta}\right) \tag{8}$$

164

165 *2.1. teady state moving point heat source*

166 Equation (8) can be solved by the assumption of the quasi-stationary condition by setting $\frac{\partial T}{\partial t} = 0$

167 [40]. Using the separation of variables, the closed form solution of the temperature field can be
168 obtained as

169

$$T = \frac{P\eta}{4\pi kR} \exp\frac{-V(R-x)}{2D} + T_0$$

170

171   (9)

172   where P is the laser power, η represents the absorption coefficient, k is thermal

173   conductivity and assumed to be temperature dependent, V is scan speed. T_0 is the initial

174   temperature.

175   R is the radial distance from the heat source which can be calculated as

176 $$R = \sqrt{x^2 + y^2 + z^2}$$

177   (10)

178   D is thermal diffusivity and can be obtained from

179 $$D(T) = \frac{k(T)}{\rho C_p^m(T)}$$

180   (11)

181   where ρ is material density and $C_p^m(T)$ is the modified heat capacity. The

182   melting/solidification phase transformation take place during AM process and it has a

183   profound effect on melt pool geometry. This is considered using modified heat capacity.

184 $$C_p^m = C_p(T) + L_f \frac{\partial f}{\partial T}$$

185   (12)

186   In which $C_p(T)$ is temperature dependent specific heat, L_f is latent heat of fusion, and f is

187   liquid fraction which can be calculated from

188
$$f = \begin{cases} 0, & T < T_s \\ \dfrac{T - T_s}{T_L - T_s}, & T_s < T < T_L \\ 1, & T > T_L \end{cases}$$

189   (13)

190

191   where, T_s is solidus temperature and T_L is liquidus temperature.

192   *2.2. Transient moving point heat source*

193   The transient point heat source solution is developed by Carslaw and Jaeger [35] using the

194   differential equation of heat conduction (Equation 8) as the following

195

196
$$T = \frac{P\eta}{8\rho C_p^m(\pi Dt)^{3/2}} \int_0^t \frac{exp\left(-\dfrac{\left((x-x') - V(t-t')\right)^2 + (y-y')^2 + (z-z')^2}{4D(t-t')}\right)}{(t-t')^{3/2}} dt' + T_0$$

197   (14)

198

199   Equation 14 gives the temperature field at position (x,y,z) at time t due to an instantaneous
200   unit heat source applied at position (x', y', z') at time t'.

201   where P is the laser power, η represents the absorption coefficient, ρ is density, C_p^m is the
202   modified heat capacity to account for solid state phase change as explained in equations 12
203   and 13. V is scan speed, D is thermal diffusivity, and T_0 is the initial temperature.

2.3. Transient semi-elliptical moving heat source

205   Three-dimensional (3D) semi-ellipsoidal heat transfer model is used to predict the temperature
206   field and melt pool geometry in metal AM processes. The proposed model can be used to predict
207   the temperature in laser-based metal additive manufacturing configurations of either direct metal
208   deposition or selective laser melting.
209   The 3D ellipsoidal heat source model is introduced by Goldak et al. [41] where the heat flux can
210   be calculated as

$$q(x,y,z) = \frac{6\sqrt{3}\,\eta P}{abc\pi\sqrt{\pi}} exp\left(-\frac{3x^2}{c^2} - \frac{3y^2}{a^2} - \frac{3z^2}{b^2}\right)$$

$$(15)$$

214   where P is the laser power, η is laser absorptivity, a, b, and c are the heat source geometry
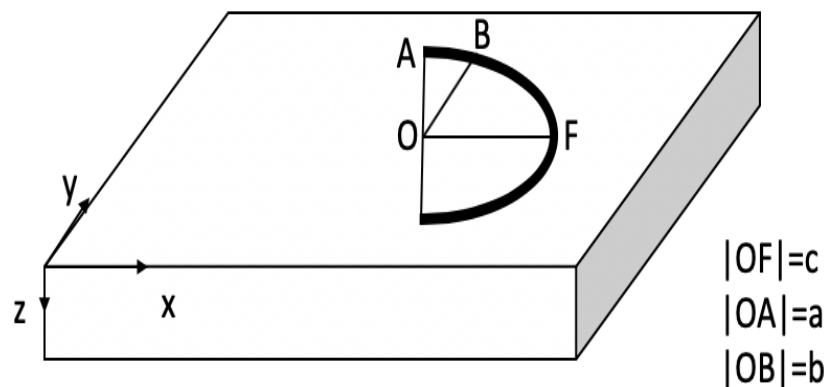215   parameters, as shown in Figure 2.

Figure 1. Heat source geometry

222   The solution of temperature for ellipsoidal moving heat source from t'=0 to t for a semi-infinite
223   body in a dimensionless form is given as [42]

$$\frac{\theta}{n} = \frac{1}{\sqrt{2\pi}}\int_0^{\frac{v^2 t}{2k}} \frac{d\tau}{\sqrt{\tau + u_a^2}\sqrt{\tau + u_b^2}}\left(\frac{A_1}{\sqrt{\tau + u_c^2}}\right)$$

225   (16)
226
227   where

$$A_1 = exp(-\frac{(\xi + \tau)^2}{2(\tau + u_c^2)} - \frac{\psi^2}{2(\tau + u_a^2)} - \frac{\lambda^2}{2(\tau + u_b^2)})$$

228
229   (17)
230
231
232   The dimensionless parameters are defined as
233

$$\xi = \frac{Vx}{2D} \ , \ \psi = \frac{Vy}{2D} , \lambda = \frac{Vz}{2D}$$

234
235   (18)
236
237   where V is scan speed, and D is thermal diffusivity which can be obtained
238   from Equation 11.
239

$$\tau = \frac{V^2(t - t')}{2D}$$

240
241   (19)
242
243
244     $$u_a = Va2\sqrt{6}\,D, \ u_b = Vb2\sqrt{6}\,D, \ u_c = Vc2\sqrt{6}\,D$$
245   (20)
246
247

$$n = \frac{P\eta V}{4\pi D^2 \rho C(T_m - T_0)}$$

248
249   (21)
250
251

$$T = \frac{P\eta V}{4\pi D^2 \rho C} \times \frac{1}{\sqrt{2\pi}} \int_0^{\frac{V^2 t}{2k}} \frac{d\tau}{\sqrt{\tau + u_a^2}\sqrt{\tau + u_b^2}} (\frac{A_1}{\sqrt{\tau + u_c^2}}) + T_0$$

252
253   (22)
254

255   *2.4. Transient double elliptical moving heat source*

256   The 3D double ellipsoidal heat source model is developed by Goldak et al. [41] as following

$$q(x,y,z,t) = \frac{6P\eta\sqrt{3}}{\pi\sqrt{\pi}\,ab} \begin{cases} \frac{f_f}{c_f} exp - 3\frac{(x - Vt)^2}{c_f^2} - 3\frac{y^2}{a^2} - 3\frac{z^2}{b^2} \quad for \ x > Vt \\ \frac{f_r}{c_r} exp - 3\frac{(x - Vt)^2}{c_r^2} - 3\frac{y^2}{a^2} - 3\frac{z^2}{b^2} \quad for \ x < Vt \end{cases}$$

257

258   (23)

259

260   where P is laser power energy, η is laser absorptivity, $a, b, c_r,$ and c_f are the respective
261   radii of the sides, rear and front of the ellipsoid as shown in Figure 3. V is the scan speed.

262   In the previous section, five different 3D heat source models known as steady state moving point
263   heat source, transient moving point heat source, transient semi-elliptical moving heat source,
264   transient double elliptical moving heat source, and uniform moving point heat source are introduced.
265   The accuracy and applicability of these models are investigated for the different range of process
266   parameters such as scan speed and laser power.   The predicted temperature field from each model
267   is validated with experimental results of the melt pool geometry.
268
269
270

271
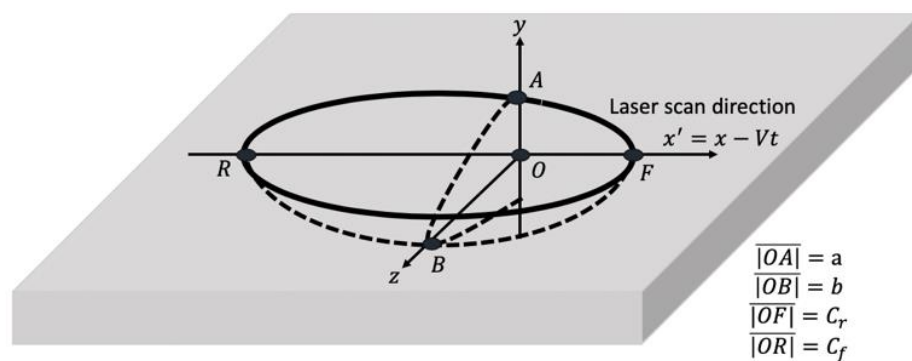
272   **Figure 2.** Illustration of the double elliptical heat source model.

273

274   f_r and f_f are the portion of the heat deposited, respectively, in the front and rear ellipsoid (with
275    $f_r + f_f = 2$). In order to fit the results to experimental data, calibration of the double-ellipsoidal heat
276   source model requires adjustment of six parameters including $\eta, a, b, c_r, c_f,$ and f_r. Some researchers
277   tried to reduce this number by applying a constraint to the model as [42-44]

$$\frac{f_f}{c_f} = \frac{f_r}{c_r}$$

279   (24)
280   This constraint guarantees the continuity of the function q across the $x = Vt$ plane at any time,
281   t, to yield

$$f_f = \frac{\alpha c_f}{c_f + c_r}$$

283   (25)
284    $\alpha = 3$ correlates to the choice of $f_f = 0.6$ as suggested by Goldak et al. [41], should be used as
285   a default value when enough experimental data are not available. It should be noted that the
286   temperature field induced by double double-ellipsoidal heat source, q, is always continuous. In
287   other words, it is independent of the value of α.
288   Green function approach is used to solve the differential equation of heat conduction (Equation
289   8) to derive the temperature field for the case of double elliptical heat source as
290

$$T(x,y,z,t) = T_0 + \frac{3P\eta\sqrt{3}}{\pi\sqrt{\pi}\,\rho C} \times \int_0^t \frac{\exp\left[-3\frac{y^2}{12D(t-t')+a^2} - 3\frac{z^2}{12D(t-t')+b^2}\right]}{\sqrt{12D(t-t')+a^2} \times \sqrt{12D(t-t')+b^2}}$$

$$\times [f_r A_r(1-B_r) + f_f A_f(1+B_f)]dt' \tag{26}$$

where

$$A_i = A(x,t,t';c_i) = \frac{\exp\left[-3\frac{(x-Vt)^2}{12D(t-t')+c_i^2}\right]}{\sqrt{12D(t-t')+c_i^2}} \tag{27}$$

$$B_i = B(x,t,t';c_i) = erf\,\frac{c_i(x-Vt)}{2\sqrt{12D(t-t')+c_i^2}\sqrt{D(t-t')}} \tag{28}$$

Equation gives the temperature field at position (x,y,z) at time t due to an instantaneous unit heat source applied at position (x',y',z') at time t'. The index i denotes front, f, or rear, r.

2.5. Transient uniform moving heat source

The heat flux $q(x,y,z)$ at any point (x,y,z) for a uniform heat source is given as [35]

$$q(x,y,z) = \frac{P\eta}{4\,abc}\begin{Bmatrix} -a < x < a \\ -b < y < b \\ 0 < z < c \end{Bmatrix} \tag{29}$$

where P is the laser power, η is laser absorptivity, a, b, and c are the heat source geometry parameters.

As for the other types of the heat sources, the solution of the temperature field is based on an instantaneous point source in a fixed coordinate

$$T = T_0 - \frac{P\eta}{2^5\rho C\,abc}\int_0^t Erfh(x+V(t-t'),a,t') \times Erfh(y,b,t')$$

$$\times Erfh(z,c,t')dt' \tag{30}$$

with Fo_s the Fourier number based on s and $t-t'$ as length and time respectively,

324
$$Erfh(x, s, t') \triangleq Erf\left(\frac{x - s}{\sqrt{4D(t - t')}}\right) - Erf\left(\frac{x + s}{\sqrt{4D(t - t')}}\right)$$

325
$$= Erf\left(\frac{\sqrt{Fo_s}}{2}\left(\frac{x}{s} - 1\right) - Erf\left(\frac{\sqrt{Fo_s}}{2}\left(\frac{x}{s} + 1\right)\right) \triangleq Erf\left(\frac{x}{s}, Fo_s\right)$$

326   (31)

3.   Results and Discussion

In the previous section, five different 3D heat source models known as steady state moving point heat source, transient moving point heat source, transient semi-elliptical moving heat source, transient double elliptical moving heat source, and uniform moving point heat source are introduced. The accuracy and applicability of these models are investigated for the different range of process parameters such as scan speed and laser power.   The predicted temperature field from each model is validated with experimental results of the melt pool geometry.

3.1.Experimental Procedure

Eight different process parameters are selected from three different literatures to validate the introduced models. The material is Ti-6Al-4V. The laser power varies from 20-500 W, the scan speed varies from 6-1200 mm/s. The process parameters are listed in Table 1.
The first four data are selected from the work of Fu et al. [37]. In this work, a continuous laser of type Nd:YAG with the wavelength of 1.06 μm is used to melt the Ti-6Al-4V metallic powders with a layer thickness of 30 μm during the single track SLM process. The wavelength of the laser and the material determine the absorption coefficient. Based on the reported wavelength and the material which is Ti-6Al-4V, the absorption coefficient would be 0.77. The laser power varies from 20 W to 80 W and the scan speed is fixed at 200 mm/s. The laser spot radius is 30 μm. The melt pool geometry is measured using optical microscopy based on the solidified microstructure.
The fifth experimental data in Table 1 is obtained from the work of Yiqun et al. [38] . In this work Ti-6Al-4V sample is built using laser melting deposition process. The laser power is 500 W and scan speed is 6 mm/s. Moreover, the layer thickness and laser spot radius are 45 μm and 26 μm, respectively. The melt pool is capture using thermal imager. More information about experimental data can be obtained in [38].
The last three experimental data are obtained from the work of Soylemez [39]. A continuous laser with a wavelength of 1.06 μm is used to build the Ti-6Al-4V parts with the fixed laser power of 300 W. The scan speed varies from 400 mm/s to 1200 mm/s. Furthermore, the layer thickness and laser spot radius are 30 μm and 50 μm, respectively. The samples are prepared using polishing and etching process to measure the melt pool geometry under an optical microscope, as illustrated in Figure 4.
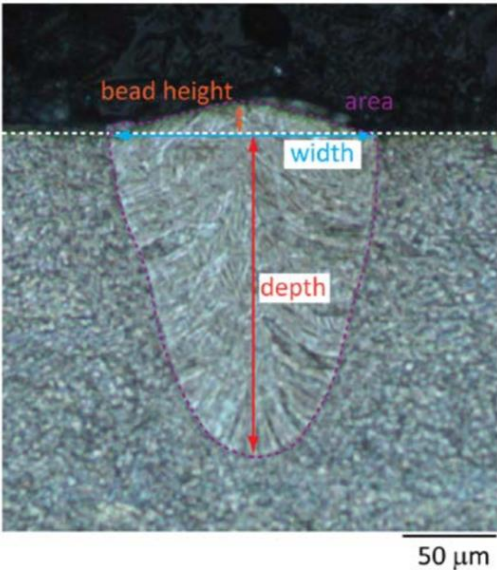
359

360   **Figure 3.** An illustration of the melt pool geometry [39].

361

362   **Table 1.** List of process parameters used for model validation.

Sample	1 [37]	2[37]	3[37]	4[37]	5[38]	6[39]	7[39]	8[39]
Laser power(W)	20	40	60	80	500	300	300	300
Scan speed (mm/s)	200	200	200	200	6	400	800	1200
Laser spot radius (μm)	26	26	26	26	26	50	50	50
Layer thickness (μm)	30	30	30	30	45	30	30	30
Absorption ratio	0.77	0.77	0.77	0.77	0.77	0.77	0.77	0.77

363

364 The wide range of process parameters are selected to validated each of the analytical models.

365

366 *3.2. Modeling Results*

367   The temperature field is predicted using five different heat source models. The predicted melt
368 pool geometry such as melt pool depth width and length is compared to experimental measurement.
369 Different combinations of laser power and scan speed are used to cover all the ranges of process
370 parameters from low to high to investigate the applicability of each model at different process
371 parameter ranges. Due to the high temperature gradient in SLM process, the thermal material
372 properties vary significantly. Therefore, the thermal material properties of the Ti-6Al-4V are
373 considered to be temperature dependent as listed in Table 2. Also, during the SLM process, the part
374 undergoes cyclic melting and solidification process, this is considered in the modeling by modifying
375 the heat capacity using latent heat of melting. Moreover, the deposition of the metallic powders layer
376 by layer could change the thermodynamic and heat transfer mechanisms. Consequently, it is
377 important to consider the layering addition in the modeling of the temperature field.

378

379

380   **Table 2.** List of temperature dependent thermal material properties of Ti-6Al-4V. (Temperature in℃)

Properties	Ti-6Al-4V

Liquidus temperature (°C)	1655
Solidus temperature (°C)	1605

Thermal conductivity (W/m°C)	
$K_s = 1.57 + 1.6 \times 10^{-2}T - 1 \times 10^{-6}T^2$	995<T<1655
$K_l = 33.4$	T=1655
$K_l = 34.6$	T=1655

Specific Heat (J/Kg°C)	
$C_p = 492.4 + 0.025T - 4.18 \times 10^{-6}T^2$	995<T<1655
$C_p = 830$	T>1655

Density (Kg/m^3)	
$\rho_s = 4.42 - 15.4 \times 10^{-2}T$	995<T<1020
$\rho_l = 3.92 - 68.0 \times 10^{-2}(T - 1020)$	T>1020

Latent heat (J/g)	286

381

382   3.2.1. Comparison of different heat source geometry

383   Figure 5 illustrates the predicted melt pool depth and width for the laser power of 20 W and the
384   scan speed of 200mm/s. The laser spot radius is 26 μm and the layer thickness is 30 μm, same as the
385   experimental procedure. Moreover, the absorption ratio is 0.77. The predicted melt pool depth and
386   width with uniform moving heat source are overestimated when compared to experimental
387   measurements. The main reason is that the geometry of the uniform heat source is more like a
388   rectangle shape as shown in Figure 6. However, the actual melt pool geometry from the experiment
389   has a circular and elliptical shape in most of the cases. Figure 7 is the same plot as Figure 5, but the
390   transient uniform heat source is omitted from the plot to better illustrate the comparison of the
391   predicted and measured melt pool depth and width for steady state point heat source (HS), transient
392   double elliptical HS, transient point HS, and transient semi-elliptical HS.
393   The predicted melt pool depth is accurately predicted with steady state point HS model and
394   transient semi-elliptical heat source. Transient double elliptical heat source has predicted the melt
395   pool depth with 12.5% error. Moreover, the transient point heat source model has predicted the melt
396   pool depth with 50% error. The reason for a high amount of error in transient heat source model is
397   that the predicted melt pool geometry is varying with time. Since this is a transient model, due to the
398   passing of time more heat would be conducted through the solid which would result in lower melt
399   pool geometry prediction. Consequently, at different time steps the melt pool geometry would vary
400   slightly. In this paper, in order to be consistent in the modeling, the predicted melt pool geometry is
401   obtained immediately after the radiation of the laser.
402   The melt pool width is also predicted for all five heat source models. The uniform heat source
403   model is predicted for all the selected process parameters in Table 1. As explained before, the
404   transient uniform HS could not predict the melt pool geometry with a reasonable range of error. Since
405   the predicted melt pool geometry using this heat source geometry is way higher than the
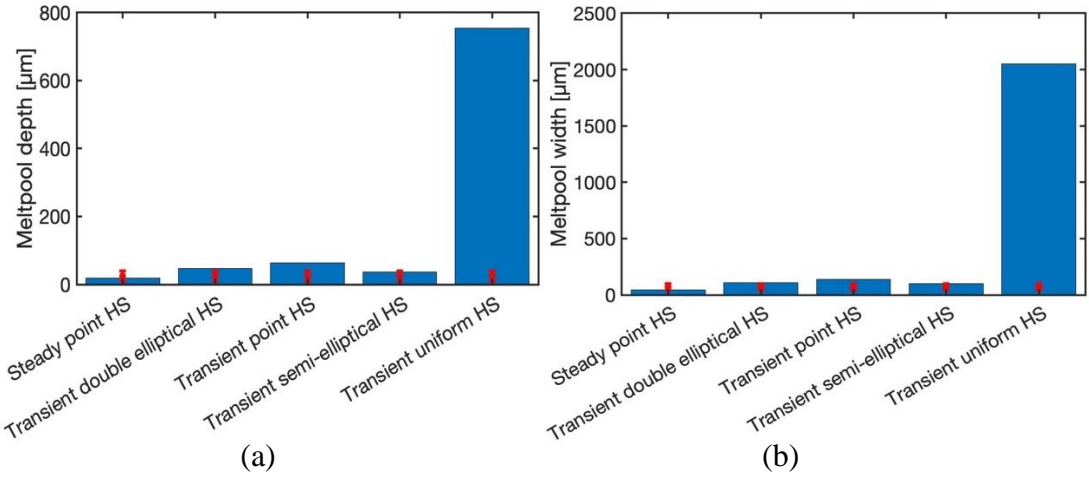406   experimental measurements, the results are not shown in this paper.

407

408

409

(a)   (b)

Figure 4. Predicted melt pool geometry with the laser power of 20 W and scan speed of 200 mm/s **(a)** melt pool depth, **(b)** melt pool width (Sample 1 in Table 1)
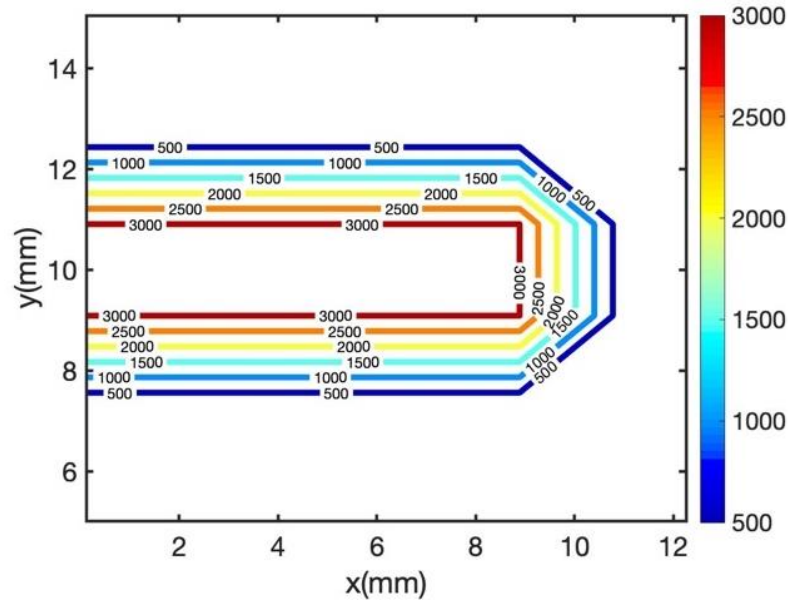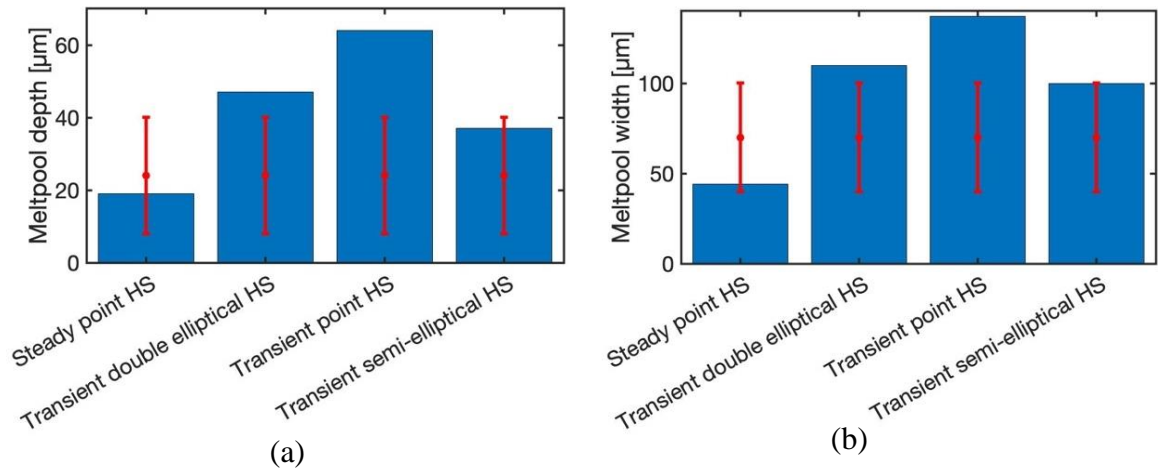

Figure 5. Illustration of the melt pool geometry using uniform moving heat source.

The melt pool width is captured by steady-state moving HS, transient double elliptical HS, transient point HS, and transient semi-elliptical HS with the maximum error of 0%, 10%, 37%, 0%, respectively.

422

423

Figure 6. Predicted melt pool geometry with the laser power of 20 W and scan speed of 200 mm/s **(a)** melt pool depth, **(b)** melt pool width (Sample 1 in Table 1)

426

427   Predicted melt pool geometry using steady state point HS, transient double elliptical HS,
428   transient point HS, and transient semi-elliptical HS for all the 8 samples are listed in Table 3.

429

430   **Table 3.** Predicted melt pool geometry for 8 different samples.

Sample	Steady state moving point HS		Transient moving point HS		Semi-elliptical HS		Double-elliptical HS		Experiment	
	Depth (μm)	Width (μm)	Depth (μm)	Width (μm)	Depth (μm)	Width (μm)	Depth (μm)	Width (μm)	Depth (μm)	Width (μm)
1	19	44	64	137	37	100	47	110	24-40[37]	70-100[37]
2	33	90	89	187	46	130	68	127	37-50[37]	80-120[37]
3	71	105	95	193	68	150	78	145	50-80[37]	110-170[37]
4	72	145	100	150	94	160	111	155	85-110[37]	140-160[37]
5	727	--	786	--	1095	--	1252	--	700-1300[38]	--
6	67	162	241	340	156	310	227	290	190-280[39]	250-300[39]
7	67	162	222	340	156	310	168	245	150-250[39]	185-225[39]
8	67	162	206	340	156	310	150	197	110-210[39]	150-200[39]

431

432   3.2.2. Region of applicability of each model based on laser power and scan speed

433   Figure 8 illustrates the predicted melt pool depth and width using steady-state moving point
434   heat source approach for different laser power and scan speed as listed in Table 1. The material for
435   all the samples is Ti-6Al-4V. Sample 1 through sample 4 is made using the laser power of 20 W, 40
436   W, 60 W and 80 W with the fixed scan speed of 200 mm/s. As shown in this figure, the predicted melt
437   pool depth and width using steady state moving point heat source approach are within the range of
438   experimental measurements. Sample 5 is built using laser power of 500 W and the scan speed of 6
439   mm/s. The predicted melt pool depth is within the range of experimental measurement. The melt
440   pool width for this sample is not reported in the literature. Sample 6 through sample 8 are built using

441   a fixed laser power of 300 W with the scan speed of 400mm/s, 800mm/s, and 1200 mm/s,
442   respectively. The predicted melt pool depth and width for these three samples are equal. The
443   predicted melt pool depth is 67 μm, and predicted melt pool width is 162 μm. This shows that the
444   steady state moving point heat source approach does not have the ability to predict the temperature
445   field for high laser speeds. This is because of the behavior of the exponential term. As the power value
446   (laser speed) of the exponential term increase, the output of the function will be less sensitive to the
447   power value. Consequently, in these cases where the magnitude of the scan speed is high, the
448   temperature field does not change.

449

450
       (a)   (b)

451
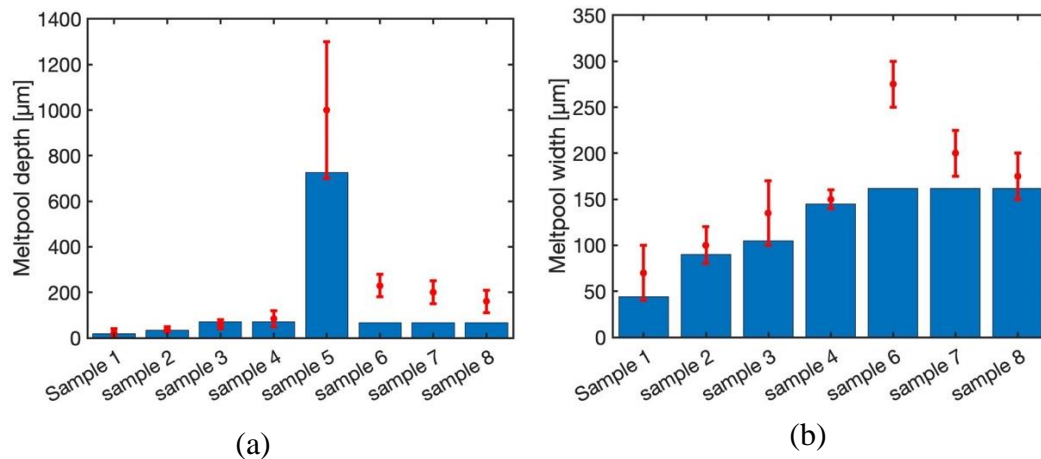
452   **Figure 7.** Predicted melt pool **(a)** depth and **(b)** width using steady state moving HS.

453   Figure 9 demonstrates the predicted melt pool geometry using the semi-elliptical heat source
454   model. Predicted melt pool width for the first four samples are within the range of experimental
455   measurements. The melt pool width and depth do not change for the samples 6 through 8. The main
456   reason could be the effect of heat source geometry. As explained by Goldak et al. [41] the heat source
457   parameters should be calibrated using experimental data. Since the goal of this work is the
458   comparison of the heat source models, the authors tried to be consistent in the modeling and
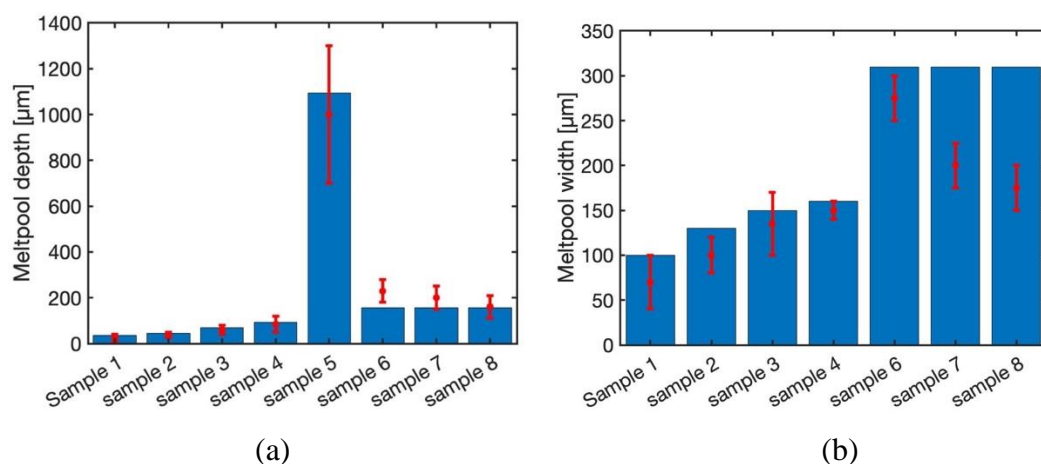459   comparison. So, the same calibration based on experimental data is used for all the samples and
460   models.

461

462
       (a)   (b)

463

464   **Figure 8.** Predicted melt pool **(a)** depth and **(b)** width using semi-elliptical moving HS

465   Figure 10 demonstrates the predicted melt pool depth and width for 8 samples using double
466   elliptical moving heat source approach. The predicted melt pool depth and width for all the samples
467   are within the range of experimental measurements. This shows that the double elliptical moving
468   heat source could be used for all the range of laser powers and scan speeds. The main reason is that
469   the actual melt pool geometry from the experimentation resembles the ellipsoidal shape.
470   Consequently, the double elliptical moving heat source could simulate the melt pool geometry quite
471   well.

(a)   (b)
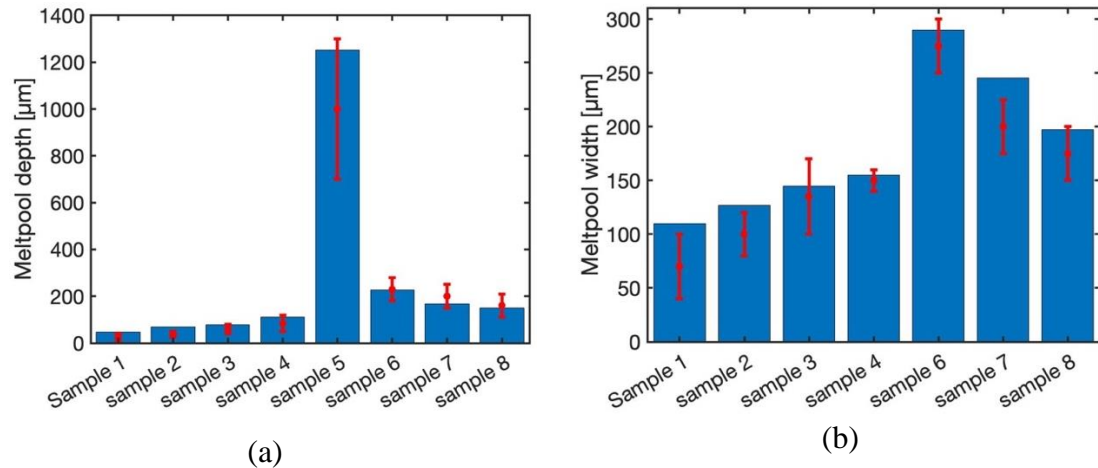
Figure 9. Predicted melt pool **(a)** depth and **(b)** width using double elliptical moving HS.

477   Figure 11 depicts the melt pool depth and width using transient moving point heat source
478   approach. The melt pool depth is well captured using this approach for all the samples. Moreover,
479   predicted melt pool width for the first four samples (sample 1 through 4) are predicted with the
480   maximum error of 15%. The predicted melt pool width for sample 6 through 8 does not change. This
481   is due to the existence of the exponential term in the modeling of the temperature field using transient
482   moving heat source approach, as explained before. As a result, the transient moving point heat source
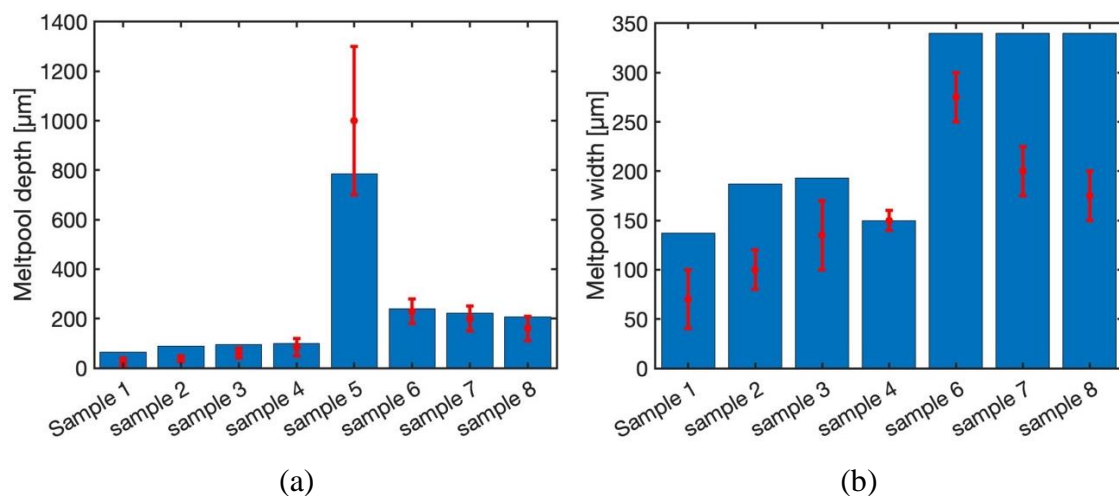483   approach could not be used for the prediction of the temperature field at high speeds.
484

(a)   (b)

Figure 10. Predicted melt pool **(a)** depth and **(b)** width using transient moving point HS

489　3.2.3. Effect of process parameters on balling effect

490　　During the SLM process, the molten powder possesses a shrinking tendency to decrease the
491　surface energy induced by surface tension [45, 46]. Thus, the balling phenomenon is very easily
492　formed during the SLM process, which is detrimental to quality of SLM processed part and impede
493　the further development of SLM technology. The balling effect hinders the quality and performance
494　of the final part due to the increase of the surface roughness. This would result in post-processing
495　procedure to polish the samples. These procedures are not only time consuming, but also costly. The
496　other disadvantageous of the balling effect during the AM process is the formation of the pores
497　between the balls which result in poor mechanical properties [47]. The balling effect could happen
498　due to two main reasons. One is the formation of the balls due to the inadequate laser energy input
499　with little liquid content. And the other due to molten pool splashes induced by high scan speed.
500　Consequently, the laser power and scan speed have a direct influence on balling effect. The balling
501　effect can be determined from the molten pool geometry. A large molten pool length to depth ratio
502　$(\frac{L}{D} > \pi)$ would result in the formation of the balls [48].

503　　In this section, the effect of process parameters such as laser power and scan speed on balling
504　effect is investigated for 8 different process parameters as listed in Table 1. As shown in Figure 12(a),
505　the balling effect is predicted using steady state moving point heat source approach. $\frac{L}{D} < \pi$ is
506　predicted for sample 1 through 5, which indicates that the process parameters are selected
507　appropriately which resulted in the formation of no balls. This is also indicated in the experimental
508　measurements. However, sample 6 through 8 experience the balling effect since the predicted
509　$\frac{L}{D}$ is greater then π. This is also observed in the experimentation as reported by Soylemez [39].

510　　Figure 12(b) illustrates the predicted balling effect using a semi-elliptical heat source model. This
511　model also correctly predicts that the first five samples do not experience the balling effect. Moreover,
512　this model predicts the formation of the balls for sample 6 through 8 due to the large molten pool
513　length to depth ratio.

514　　Figure 12(c) and Figure 12(d) depict the predicted balling effect employing a double elliptical
515　heat source model, and transient moving point heat source model, respectively. Both of these models
516　accurately predict no formation of the balls for the first five samples, and formation of the balls for
517　sample 6 through 8.

518　　As shown in these figures, the combination of process parameters such as scan speed and laser
519　power have a substantial effect on the formation of the balls. The process parameters can be
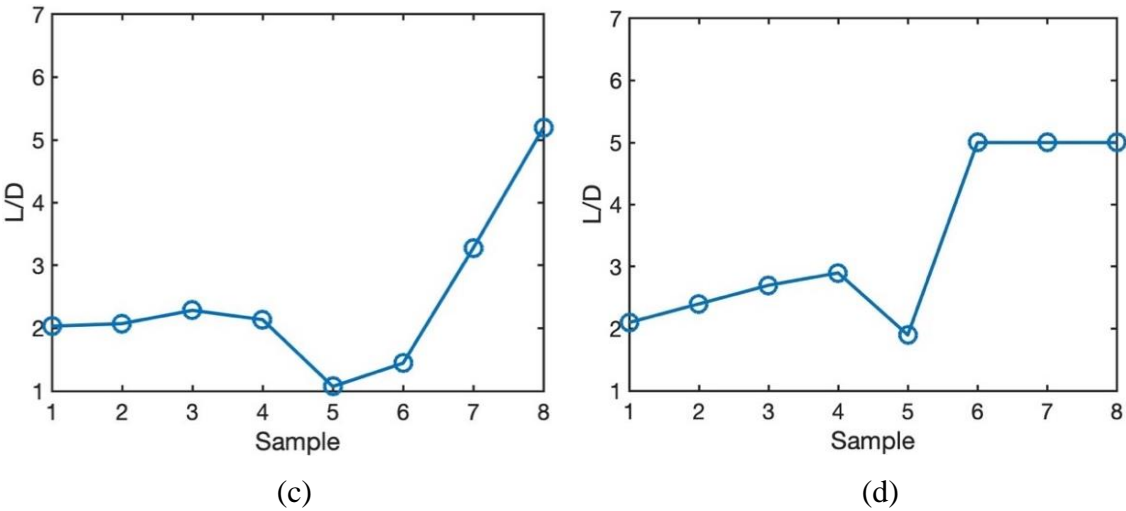520　optimized to prevent any formation of the balls during the AM process.

521

522

523　　　　　　　　　　　　　　　　(a)　　　　　　　　　　　　　　　　　　　　　(b)

(c)   (d)
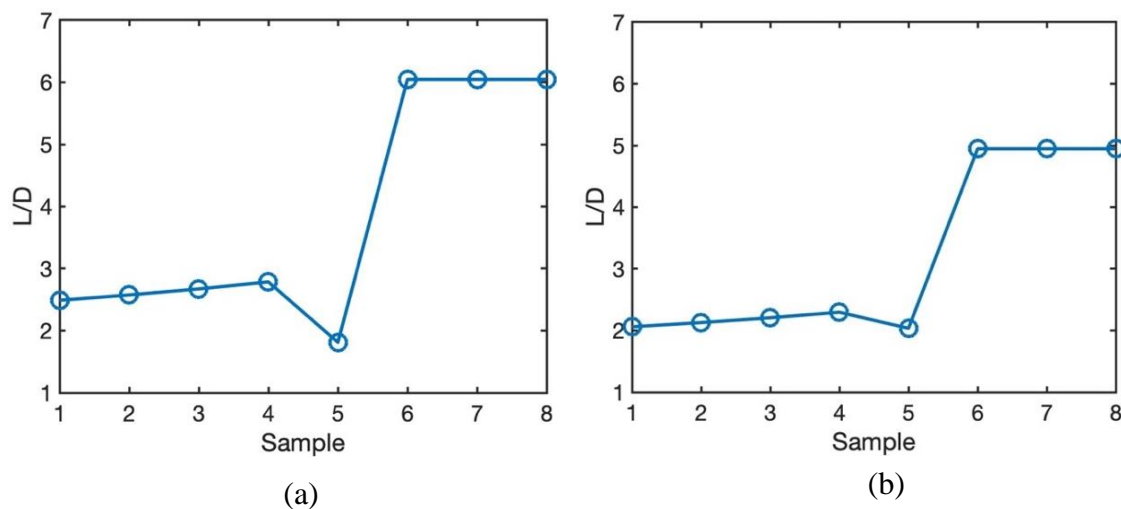
Figure 11. prediction of balling for 8 different samples as listed in Table 1 using **(a)** steady state moving point heat source, **(b)** semi-elliptical moving heat source, **(c)** double elliptical moving heat source, and **(d)** transient moving point heat source.

4.   Conclusion

The laser-matter interaction is a crucial physical phenomenon in the SLM process. In this paper, five different heat source models known as steady state moving point heat source, semi-elliptical moving point heat source, double elliptical moving point heat source, transient moving point heat source, and uniform moving heat source are introduced to predict the in- process temperature field in SLM process for Ti-6Al-4V samples. Due to the large temperature gradient during the SLM process, the magnitude of the thermal material properties varies significantly. As a result, the material properties are considered to be temperature dependent. Moreover, the build part undergoes cyclic melting and solidification process which impacts the temperature field. Consequently, the solid-state phase change is considered by modifying the heat capacity using latent heat of melting. During the SLM process, the part is built layer by layer. This would have a substantial impact on heat transfer mechanisms. Accordingly, the effect of layering addition is also considered by considering the temperature history and interaction of the layers in the modeling of the temperature field using five different approaches. Predicted melt pool geometry from these models are compared to experimental work. Wide range of process parameters is selected to determine the capability of each of models. The laser power varies from 20 W to 500 W, and the scan speed varies from 6 mm/s to 1200 mm/s.

The predicted melt pool geometry using uniform moving heat source is way above the experimental measurements. This is due to the fact the uniform heat source resembles a rectangle shape. However, the actual molten pool geometry from the experiments is more like an elliptical shape or a circle shape.

The steady-state moving point heat source, semi-elliptical heat source, and transient moving point heat source could predict the melt pool geometry quite well for low and medium scan speeds. However, at high speeds, no changes in melt pool geometry are observed. This is due to the behavior of the exponential term in the modeling of these heat sources.

The double elliptical model could predict the melt pool geometry for all the ranges of the process parameters. This is due to the fact that the double elliptical heat source resembles the actual melt pool geometry from experimentation. As a result, it can predict the temperature field quite well.

Furthermore, the effect of process parameters on the balling effect is investigated. Steady-state moving point heat source, semi-elliptical moving point heat source, double elliptical moving point heat source, and transient moving point heat source models are used to predict the formation of the balls in SLM process. All the models could predict the formation of the balls for 8 different samples. The results are also compared to the explained experimental work from the literature. It is shown that the combination of scan speed and the laser power is the main reason for the existence of the

562   balls. Consequently, these process parameters should be selected in a way to prevent any formation
563   of the balls.
564

570   **References**

571   1.   Bikas, H., P. Stavropoulos, and G. Chryssolouris, *Additive manufacturing methods and modelling approaches: a*
572   *critical review.* The International Journal of Advanced Manufacturing Technology, 2016. **83**(1-4): p. 389-405.
573   2.   Mirkoohi, E. *Effect of particle shape on neck growth and shrinkage of nanoparticles.* in *2017 Manufacturing Science*
574   *and Engineering Conference.* 2017.
575   3.   Yang, Y., *Temperature-Dependent Thermoelastic Analysis of Multi-Dimensional Functionally Graded Materials.*
576   2016, University of Pittsburgh.
577   4.   Clijsters, S., et al., *In situ quality control of the selective laser melting process using a high-speed, real-time melt pool*
578   *monitoring system.* The International Journal of Advanced Manufacturing Technology, 2014. **75**(5-8): p. 1089-
579   1101.
580   5.   Craeghs, T., et al., *Determination of geometrical factors in Layerwise Laser Melting using optical process*
581   *monitoring.* Optics and Lasers in Engineering, 2011. **49**(12): p. 1440-1446.
582   6.   Mendez, P.F., Y. Lu, and Y. Wang, *Scaling analysis of a moving point heat source in steady-state on a semi-infinite*
583   *solid.* Journal of Heat Transfer, 2018. **140**(8): p. 081301.
584   7.   Gebhardt, A., et al., *Additive manufacturing by selective laser melting the realizer desktop machine and its*
585   *application for the dental industry.* Physics Procedia, 2010. **5**: p. 543-549.
586   8.   Lim, S., et al., *Developments in construction-scale additive manufacturing processes.* Automation in construction,
587   2012. **21**: p. 262-268.
588   9.   Rüßmann, M., et al., *Industry 4.0: The future of productivity and growth in manufacturing industries.* Boston
589   Consulting Group, 2015. **9**(1): p. 54-89.
590   10. Mirkoohi, E., P. Bocchini, and S.Y. Liang, *Inverse analysis of residual stress in orthogonal cutting.* Journal of
591   Manufacturing Processes, 2019. **38**: p. 462-471.
592   11. Ganeriwala, R., et al., *Evaluation of a thermomechanical model for prediction of residual stress during laser powder*
593   *bed fusion of Ti-6Al-4V.* Additive Manufacturing, 2019. **27**: p. 489-502.
594   12. Tabei, A., et al., *Modeling of texture development in additive manufacturing of Ni-based superalloys.* The
595   International Journal of Advanced Manufacturing Technology, 2019.
596   13. Zhao, X., et al., *Numerical modeling of the thermal behavior and residual stress in the direct metal laser sintering*
597   *process of titanium alloy products.* Additive Manufacturing, 2017. **14**: p. 126-136.
598   14. Mirkoohi, E., P. Bocchini, and S.Y. Liang, *An analytical modeling for process parameter planning in the machining*
599   *of Ti-6Al-4V for force specifications using an inverse analysis.* The International Journal of Advanced
600   Manufacturing Technology, 2018. **98**(9-12): p. 2347-2355.
601   15. Feng, Y., et al., *Inverse Analysis of Inconel 718 Laser-Assisted Milling to Achieve Machined Surface Roughness.*
602   International Journal of Precision Engineering and Manufacturing, 2018. **19**(11): p. 1611-1618.
603   16. Feng, Y., et al., *Surface roughness modeling in Laser-assisted End Milling of Inconel 718.* Machining Science and
604   Technology, 2019: p. 1-19.
605   17. Zeng, K., D. Pal, and B. Stucker. *A review of thermal analysis methods in laser sintering and selective laser melting.*
606   in *Proceedings of Solid Freeform Fabrication Symposium Austin, TX.* 2012.
607   18. Bugeda Miguel Cervera, G. and G. Lombera, *Numerical prediction of temperature and density distributions in*
608   *selective laser sintering processes.* Rapid Prototyping Journal, 1999. **5**(1): p. 21-26.
609   19. Loh, L.-E., et al., *Numerical investigation and an effective modelling on the Selective Laser Melting (SLM) process*
610   *with aluminium alloy 6061.* International Journal of Heat and Mass Transfer, 2015. **80**: p. 288-300.
611   20. Mirkoohi, E., P. Bocchini, and S.Y. Liang, *Analytical temperature predictive modeling and non-linear optimization*
612   *in machining.* The International Journal of Advanced Manufacturing Technology, 2019: p. 1-10.

613 21. Mirkoohi, E., P. Bocchini, and S.Y. Liang, *An Analytical Modeling for Designing the Process Parameters for*
614   *Temperature Specifications in Machining.* 2018.
615 22. Feng, Y., et al., *Inverse analysis of the cutting force in laser-assisted milling on Inconel 718.* The International
616   Journal of Advanced Manufacturing Technology, 2018. **96**(1-4): p. 905-914.
617 23. Chiumenti, M., et al., *Numerical modelling and experimental validation in Selective Laser Melting.* Additive
618   manufacturing, 2017. **18**: p. 171-185.
619 24. Denlinger, E.R., et al., *Thermal modeling of Inconel 718 processed with powder bed fusion and experimental*
620   *validation using in situ measurements.* Additive Manufacturing, 2016. **11**: p. 7-15.
621 25. Rodriguez, E., et al., *Approximation of absolute surface temperature measurements of powder bed fusion additive*
622   *manufacturing technology using in situ infrared thermography.* Additive Manufacturing, 2015. **5**: p. 31-39.
623 26. Fischer, P., et al., *Temperature measurements during selective laser sintering of titanium powder.* International
624   Journal of Machine Tools and Manufacture, 2004. **44**(12-13): p. 1293-1296.
625 27. Everton, S.K., et al., *Review of in-situ process monitoring and in-situ metrology for metal additive manufacturing.*
626   Materials & Design, 2016. **95**: p. 431-445.
627 28. Andreotta, R., L. Ladani, and W. Brindley, *Finite element simulation of laser additive melting and solidification*
628   *of Inconel 718 with experimentally tested thermal properties.* Finite Elements in Analysis and Design, 2017. **135**:
629   p. 36-43.
630 29. Roberts, I.A., et al., *A three-dimensional finite element analysis of the temperature field during laser melting of metal*
631   *powders in additive layer manufacturing.* International Journal of Machine Tools and Manufacture, 2009.
632   **49**(12-13): p. 916-923.
633 30. Antony, K., N. Arivazhagan, and K. Senthilkumaran, *Numerical and experimental investigations on laser*
634   *melting of stainless steel 316L metal powders.* Journal of Manufacturing Processes, 2014. **16**(3): p. 345-355.
635 31. Wessels, H., et al., *Investigation of heat source modeling for selective laser melting.* Computational Mechanics,
636   2018: p. 1-22.
637 32. Mirkoohi, E., et al., *Thermal modeling of temperature distribution in metal additive manufacturing considering*
638   *effects of build layers, latent heat, and temperature-sensitivity of material properties.* Journal of Manufacturing and
639   Materials Processing, 2018. **2**(3): p. 63.
640 33. Pinkerton, A.J. and L. Li, *The significance of deposition point standoff variations in multiple-layer coaxial laser*
641   *cladding (coaxial cladding standoff effects).* International Journal of Machine Tools and Manufacture, 2004.
642   **44**(6): p. 573-584.
643 34. Peyre, P., et al., *Analytical and numerical modelling of the direct metal deposition laser process.* Journal of Physics
644   D: Applied Physics, 2008. **41**(2): p. 025403.
645 35. Carslaw, H.S. and J.C. Jaeger, *Conduction of heat in solids.* Oxford: Clarendon Press, 1959, 2nd ed., 1959.
646 36. Paul, R. and S. Anand, *Process energy analysis and optimization in selective laser sintering.* Journal of
647   Manufacturing Systems, 2012. **31**(4): p. 429-437.
648 37. Fu, C. and Y. Guo, *Three-dimensional temperature gradient mechanism in selective laser melting of Ti-6Al-4V.*
649   Journal of Manufacturing Science and Engineering, 2014. **136**(6): p. 061004.
650 38. 李俐群, et al., *Ti6Al4V 激光熔化沉积熔池温度场与微观组织特性.* 中国激光, 2017. **44**(3): p. 113-120.
651 39. Soylemez, E., *MODELING THE MELT POOL OF THE LASER SINTERED TI6AL4V LAYERS WITH*
652   *GOLDAK'S DOUBLE-ELLIPSOIDAL HEAT SOURCE.*
653 40. Carslaw, H. and J. Jaeger, *Conduction of heat in solids: Oxford Science Publications.* 1959: Oxford, England.
654 41. Goldak, J., *A double ellipsoid finite element model for welding heat sources.* IIW Doc. No., 1985. **212**.
655 42. Nguyen, N., et al., *Analytical solutions for transient temperature of semi-infinite body subjected to 3-D moving heat*
656   *sources.* WELDING JOURNAL-NEW YORK-, 1999. **78**: p. 265-s.
657 43. Lundbäck, A., H. Alberg, and P. Henrikson. *Simulation and validation of TIG-welding and post weld heat*
658   *treatment of an Inconel 718 plate.* in *International Seminar on Numerical Analysis of Weldability: 29/09/2003-*
659   *01/10/2003.* 2005. Techn. Univ. TYG.
660 44. Nguyen, N., et al., *Analytical Approximate Solution for Double Ellipsoidal Heat Source in Finite Thick Plate.*
661   Welding Journal, 2004. **83**(3): p. 82.
662 45. Kruth, J.-P., et al., *Selective laser melting of iron-based powder.* Journal of materials processing technology,
663   2004. **149**(1-3): p. 616-622.
664 46. Gu, D. and Y. Shen, *Balling phenomena during direct laser sintering of multi-component Cu-based metal powder.*
665   Journal of Alloys and Compounds, 2007. **432**(1-2): p. 163-166.

666   47.   Li, R., et al., *Densification behavior of gas and water atomized 316L stainless steel powder during selective laser*
667   *melting.* Applied surface science, 2010. **256**(13): p. 4350-4356.
668   48.   Gu, D. and Y. Shen, *Balling phenomena in direct laser sintering of stainless steel powder: Metallurgical mechanisms*
669   *and control methods.* Materials & Design, 2009. **30**(8): p. 2903-2910.

670

671